

Spatiotemporal Characteristics and Pressure Fluctuations of Internal Flow in a High-Speed Centrifugal Blower for Vacuum Cleaner at Low Flow-Rate Conditions

Y. Chen, Z. Wang, H. Yang[†], W. Zhang and Y. Wei

Key Laboratory of Fluid Transmission Technology of Zhejiang Province, Zhejiang Sci-Tech University, Hangzhou, Zhejiang 310018, China.

[†]Corresponding Author Email: yanghui@zstu.edu.cn

(Received April 17, 2022; accepted September 30, 2022)

ABSTRACT

The steady and unsteady characteristics of the internal flow in a high-speed centrifugal blower are studied by computational fluid dynamics (CFD) approach at low flow rates. It is demonstrated that as the flow rate decreases, the separation of flow in the blade passage becomes serious, and separated vortices always occur on the suction surface of the blade which gradually expand and block the passage. The stall cells move downstream and generate vortices at the exit of the passage, resulting serious loss to the performance of the blower. Q-criteria is used to analyze the flow field and explore the evolution of the vortex structure in the impeller. It is further found that strong pressure fluctuations are caused by the rotating stall in the impeller. At the stall conditions, the instability characteristics are particularly obvious. At flow rates of $0.65Q_n$ and $0.47Q_n$, the pressure fluctuation in the blade passage is dominated by the blade passing frequency, while a lower frequency dominates at $0.26Q_n$. Moreover, the flow on the suction surface of impeller blades fluctuates substantially. The characteristics of steady flow and unsteady flow can clearly explain the internal flow of centrifugal blower for vacuum cleaners at low-flow conditions, which can be widely used in various engineering designs of vacuum cleaners.

Keywords: Centrifugal blower; Unsteady flow; Rotating stall; Spatiotemporal characteristics; Pressure fluctuations

NOMENCLATURE

B	width	S	source term
c	velocity	t	time
C_p	heat capacity	T	integral time scale
C_μ	turbulent constant	\mathbf{u}	velocity
D	diameter	α	angle
G	turbulent kinetic energy	β	coefficient of expansion
K	heat transfer coefficient	η	variable efficiency
m	polytropic index	ρ	fluid density
P	pressure	μ	viscosity
R	air gas constant	μ_t	turbulent viscosity

1. INTRODUCTION

Vacuum cleaner is widely applied in the daily life. A high-speed centrifugal blower is the core element of vacuum cleaner suction, and its performance plays a key role in the quality of vacuum cleaner products. The internal flow structure of the centrifugal blower exerts an enormous function on improving the

performance of vacuum cleaner. Thus, to improve and optimize the efficiency of centrifugal blower is of great significance to realize the purpose of energy conservation. The centrifugal blower with a wide range of working conditions and high operation efficiency becomes an inevitable trend of the industry development (Shen *et al.* 2019). According to Zhou *et al.* (2018), when the centrifugal impeller is

alternately stalled, the pressure fluctuation amplitude is significantly smaller than the rotating stall fluctuation amplitude. Propagating of the stall cells has a significant effect on the pressure fluctuations of the impeller. Three-dimensional numerical simulations of the backward curved blade centrifugal fan are performed to explore the aerodynamic and aero-acoustic characteristics at the Best Efficiency Point (BEP) and $1.3 \times \text{BEP}$ flow conditions by Zhang *et al.* (2016). The intensity and location of the aero-acoustic sources are determined by using the URANS method. As described by Yang *et al.* (2013), numerical simulation of unstable internal flow is carried out in centrifugal fan. It is figured out that the interaction between the fixed volute and the non-uniform flow of impeller aroused the notable pressure fluctuations, which is the main source of vibration and noise. Younsi *et al.* (2007) studied the complex phenomenon of unsteady flow in centrifugal fan by CFD. The phenomenon studied were the interaction and instability caused by the motion of the rotating blade relative to the volute and their effect on the air-acoustic behavior of the fan. The effects of inlet recirculation arrangement on the stall of the deflector and the width of the diffuser on the stall of the high-specific-speed centrifugal impeller with deflector are analyzed by numerical simulation with experimental verification (Ishida *et al.* 2005). Gao and Zhong (2012) illustrated the underlying cause of the periodic pressure fluctuations, and introduced the evolution of the formation and disappearance of the separated vortices within the impeller. Chun *et al.* (2011) conducted studies on the surge and stall caused by the interaction of parallel axial fans in the tunnel. It is proved that once a stall occurs, the noise will suddenly increase, which will cause the fan to vibrate and run unstable. Several scholars argued that the mechanical damage and major failures are mainly caused by the rotating stalls (Zhang *et al.* 2019a; Sundstrm *et al.* 2018; Sandra *et al.* 2005).

However, the current research on centrifugal blower for vacuum cleaner is not in-depth, domestic and foreign scholars mainly discuss the centrifugal impeller modification, noise reduction to improve the efficiency of the fan. Park *et al.* (2008) found that the vacuum cleaner centrifugal impeller has a streamlined blade shape, and its efficiency can be increased by about 4.2% when the blade outlet is bend by about $20^\circ \sim 25^\circ$. Zhang *et al.* (2013) studied the influence of half-height diffuser blade height on the aerodynamic performance of centrifugal fans for vacuum cleaners. The simulation results show that the half-height diffuser can better improve the flow field in the diffuser, and the fan efficiency reaches the maximum value under the half-height diffuser with the blade height $h/b=0.4-0.6$. Ming *et al.* (2018) took the high-speed centrifugal fan for vacuum cleaner as the optimization object, and replaced the vane-less diffuser with a vane diffuser to improve the energy recovery efficiency in the diffuser. After optimization, the efficiency at the design point of the whole machine is increased by 6.6%, and the vacuum degree is increased by 7.6%. Besides, Bai and Song (2020) simulated and analyzed the internal flow field of the electric fan of the multi-stage vacuum cleaner, and studied the influence of different factors on the

electric fan of the vacuum cleaner. It is concluded that the higher the number of stages of the fan, the greater the degree of vacuum and the higher the speed of the impeller, the greater the degree of vacuum.

In reality, vacuum cleaner with centrifugal impeller is often run in the high speed with low flow rates conditions, to achieve high vacuum degree with large suction. Therefore, it is particularly important to research the internal flow and its evolution mechanism of centrifugal blower for vacuum cleaner at low flow rates.

In this paper, a centrifugal blower for vacuum cleaner is studied with a rotational speed up to 70,000 rpm. We mainly focus on the steady flow and unsteady flow characteristics of impeller and diverter at low flow rates. The origin and effect of flow velocity reduction on internal flow, as well as the fluctuation spectral analysis of pressure, are deeply studied to provide some physical insights into understanding the rotating stall mechanism of centrifugal blower. The main framework of this paper is divided into several parts. Section 2 mainly describes the governing equations and numerical method. The numerical results and discussions of steady and unsteady flow are presented in Section 3. In final, some constructive conclusions are summarized.

2. GOVERNING EQUATIONS AND NUMERICAL METHOD

2.1 Research Model

The geometry structure of the centrifugal blower for the vacuum cleaner in this paper is shown in Fig. 1. The centrifugal blower model is composed of impeller, flow diverter and axis. Table 1 shows the main parameters of the blower.

Table 1. Main geometric parameters of the centrifugal blower

Parameters	values
Impeller inlet diameter (D_1)	16mm
Impeller outlet diameter (D_2)	44mm
Impeller outlet width (B_1)	5mm
Blade inlet angle (α_1)	77.2°
Blade outlet angle (α_2)	24.1°
Number of blades (Z)	11
Flow diverter width (B_2)	25mm



Fig. 1. Geometric model of the centrifugal blower.

2.2 Governing Equations of Fluid Flow

The three physical conservation laws of mass, momentum and energy are those followed by all natural movements. The mathematical description of these three physical laws in fluid motion is described as continuity equation, momentum equation and energy equation (Yang *et al.* 2019; Wei *et al.* 2019; Wang *et al.* 2020; Zhang *et al.* 2019b). In the numerical calculation of 3D flow of centrifugal blower, the compressible flow is implemented and the equations needed to be solved are as follows:

The continuity equation is:

$$\frac{\partial \rho}{\partial t} + \frac{\partial}{\partial x_i}(\rho u_i) = 0 \quad (1)$$

The momentum equation is:

$$\frac{\partial}{\partial t}(\rho u_i) + \frac{\partial}{\partial x_j}(\rho u_i u_j) = -\frac{\partial P}{\partial x_i} + \frac{\partial}{\partial x_j}(\mu \frac{\partial u_i}{\partial x_j} - \overline{\rho u_i u_j}) + S_i \quad (2)$$

where u_i and u_j are the velocity in different directions, and $-\overline{\rho u_i u_j}$ characterizes the amount of correlation between turbulent stress fluctuation intensity.

The energy equation is:

$$\frac{\partial(\rho u_i T)}{\partial x_j} = \frac{\partial}{\partial x_j} \left(\frac{K}{C_p} \frac{\partial T}{\partial x_j} \right) + S_T \quad (3)$$

where S_T refers to the internal heat source of the fluid medium and the part where the mechanical energy of the fluid medium is converted into heat energy due to viscosity.

In this paper, steady numerical simulations are implemented by a standard k-ε turbulence model. The standard k-ε model is currently the most widely used algorithmic model, which introduces the turbulent kinetic energy and the turbulent dissipation rate, and links the turbulent viscosity coefficient and the fluctuation kinetic energy as well as the fluctuation characteristic scale (Wolfram and Carolus 2012). The standard k-ε model is:

$$\rho \frac{Dk}{Dt} = \frac{\partial}{\partial x_i} \left[\left(\mu + \frac{\mu_t}{\sigma_k} \right) \frac{\partial k}{\partial x_i} \right] + G_k + G_b - \rho \varepsilon \quad (4)$$

$$\rho \frac{D\varepsilon}{Dt} = \frac{\partial}{\partial x_i} \left[\left(\mu + \frac{\mu_t}{\sigma_\varepsilon} \right) \frac{\partial \varepsilon}{\partial x_i} \right] + C_{1\varepsilon} \frac{\varepsilon}{k} (G_k + G_{sb} G_b) - C_{2\varepsilon} \rho \frac{\varepsilon^2}{k} \quad (5)$$

where μ_t denotes the turbulent viscosity coefficient $\mu_t = \rho C_\mu \frac{k^2}{\varepsilon}$, C_μ is the turbulent constant, G_k represents the generation of turbulent kinetic energy caused by the average velocity gradient, $G_k = \mu_t \left(\frac{\partial u_i}{\partial x_j} + \frac{\partial u_j}{\partial x_i} \right) \frac{\partial u_i}{\partial x_j}$, G_b denotes the generation of turbulent kinetic energy caused by the influence of buoyancy $G_b = \beta g_i \frac{\mu_t}{Pr_i} \frac{\partial T}{\partial x_i}$, where β is the coefficient of expansion, $\beta = -\frac{1}{\rho} \frac{\partial \rho}{\partial T}$.

The large eddy simulation (LES) turbulence model is used for the unsteady numerical simulation. Compared with the direct numerical simulations, the LES reduces the requirements of the computer operation speed and capacity and obtaining the information of the turbulent motion flow field is more comprehensive, which has a promising development prospect (Borello *et al.* 2013; Gan *et al.* 2008; Zhang *et al.* 2011). The control equation for the LES is to consider the Navier-Stokes equation in the spatial domain. The small-scale vortexes are removed by the LES, and the equations are obtained:

$$\frac{\partial \rho}{\partial t} + u \frac{\partial \rho u_i}{\partial x_i} = 0 \quad (6)$$

$$\frac{\partial}{\partial t}(\rho \overline{u_i}) + \frac{\partial}{\partial x_j}(\rho \overline{u_i u_j}) = \frac{\partial}{\partial x_j} \left(\mu \frac{\partial \overline{u_i}}{\partial x_j} \right) - \frac{\partial \overline{p}}{\partial x_j} - \frac{\partial \tau_{ij}}{\partial x_j} \quad (7)$$

where $\tau_{ij} = \overline{\rho u_i u_j} - \rho \overline{u_i} \cdot \overline{u_j}$ denotes sub-grid stress.

2.3 Mesh and Its Independence Study

The centrifugal blower was simplified appropriately, removing the frame, motor, threaded holes and flanges in the CFD. In addition to the impeller and the diversion need to divide the mesh, in order to set the boundary conditions accurately, it is also necessary to make certain extension of the inlet and outlet. As shown in Fig. 2a, the fluid domain is ultimately divided into four parts: inlet extension domain, impeller domain, deflector domain, and outlet extension domain. Considering the structural complexity of impeller and flow diverter, the mesh is filled with unstructured tetrahedron. The structure grid division is performed for the inlet and outlet extension section. At the same time, to calculate more accurately, the local mesh encryption was carried out for narrow areas (leading edge and trailing edge of blade) and the near-wall area of the blade surface in the model. The mesh division of the model is shown in Fig. 2b.

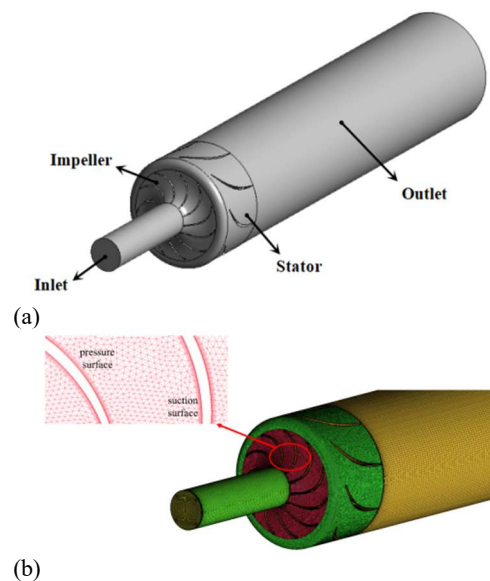


Fig. 2. Model of fluid domain and mesh generation: (a) Model of fluid domain, (b) Mesh generation.

In order to select the appropriate number of grids, grid independence verification is required. In this paper, six groups of grids with different numbers are calculated under the same conditions, and the results are shown in Fig. 3. The results show that when the grid number increases from 4.7 million to 9.2 million, the relative variations of the vacuum degree and the variable efficiency are 0.81% and 0.76%, respectively. Therefore, the elements of 4.7 million are used for the subsequent simulation. Table 2 shows the number of grids for each fluid domain.

Table 2. Number of grids in each domain

Component	Number of Grids (10 ⁴)
Inlet duct domain	17.1
Outlet duct domain	20.5
Impeller domain	230.2
Flow diverter domain	201.5
Total	469.3

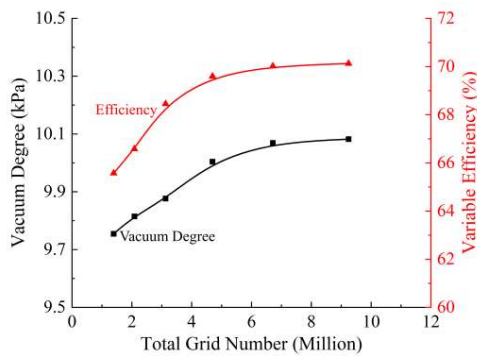


Fig. 3. Grid dependence test.

2.4 Simulation Settings

ANSYS CFX17.0 software is used in all numerical simulations. All conditions of numerical simulation are as follows:

-Standard k-ε turbulence model and the SIMPLE (Semi-Implicit Method for Pressure Linked Equations) algorithm are used for steady simulation.

-The fluid medium is ideal gas and the reference pressure is 0 Pa.

-Total pressure is used in the inlet boundary condition; pressure and temperature are set as 101325 Pa, 288.18K, respectively. And static pressure is selected in the outlet boundary condition. The flow rate of the blower is changed by adjusting the static pressure value of the outlet.

-The impeller rotates at the speed of 70000 rpm and takes the z-axis as the rotation axis.

-The conditions of non-sliding and adiabatic are adopted in the wall boundary.

-The unsteady numerical simulation is carried out based on the steady results. The independence of time step is performed at the rated operating conditions. The results display that when the time steps are less than 4.7619×10⁻⁶s, they have almost no effect on the vacuum degree and efficiency, respectively. Taken together, the subsequent

unsteady simulations used a time step of 4.7619×10⁻⁶s, with a rotation angle equal to 2°. 20 revolutions are simulated and the last revolution is used for analysis.

3. RESULTS AND DISCUSSIONS

3.1 External Characteristics of Centrifugal blower

The general regularities of static pressure and variable efficiency of this centrifugal blower with flow coefficient are concluded by the analysis and numerical simulation of various working conditions, as is shown in Fig. 4. Q_n is the highest efficiency point on the performance curve of the blower, that is the rated working condition, Q_n=18.58L/s. The abscissa is represented by Q/Q_n. The variable efficiency is defined as:

$$\eta = \frac{\frac{m}{m-1} RT_1 \left[\left(\frac{P_2}{P_1} \right)^{\frac{m-1}{m}} - 1 \right] + \frac{c_2^2 - c_1^2}{2}}{\frac{c_2^2 - c_1^2}{2} + C_p(T_2 - T_1)} \quad (8)$$

where *m* is the polytropic index, *R* is the air gas constant with a value of 287, J/(mol·K); *C_p* is constant pressure specific heat of air, J/(kg·K); And *P₁*, *T₁*, *c₁*, *P₂*, *T₂*, *c₂* represent inlet static pressure, Pa; inlet temperature, K; inlet velocity, m/s; outlet static pressure, Pa; outlet temperature, K; outlet velocity, m/s, respectively.

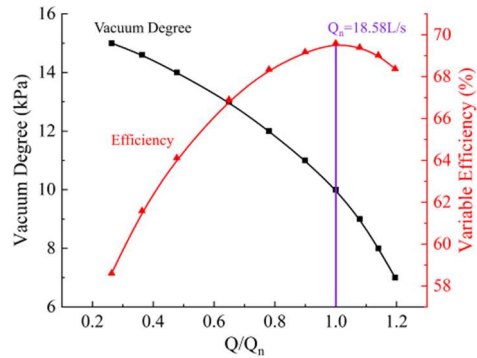


Fig. 4. External characteristic curves of centrifugal blower.

It is obtained in Fig. 4 that the vacuum degree increases with the decrease of the flow rate, and the growth rate gradually slows down. The variable efficiency of the blower is issued by 69.59% at the rated working condition and maintains high efficiency in a range of 0.8~1.2 Q/Q_n. When Q/Q_n is lower than 0.8, the variable efficiency of the static pressure gradually decreases. The leakage loss and impeller resistance loss will increase when too small flow. Especially in the flow is less than 0.65Q_n, the impeller internal gradually occurs rotation stall. Due to increasing positive rush angle, this will cause serious flow separation, even though that generate revolving loss speed appearance, this cause surge and

ultimately undermine effectiveness. On the other hand, because gas motion rub loss and impact loss increasing when too large flow, exceed a certain range then will cause that blade surface will happen flow separation, even though happen block. It will also cause the decrease of blower efficiency. Therefore, the flow rate of less than $0.65Q_n$ is defined as a low flow rate condition in this paper. And the blower used for the vacuum cleaner is also operated in this environment. Three low-flow operating conditions of $0.65Q_n$, $0.47Q_n$ and $0.26Q_n$ are selected for the study.

3.2 Steady Flow Characteristics at Different Working Conditions

To effectively capture the complex features of internal flow in centrifugal blower, the pressure, velocity and streamline are described at the same plane at different working conditions, respectively. Fig. 5 shows the locations of section I at half height of the impeller outlet.

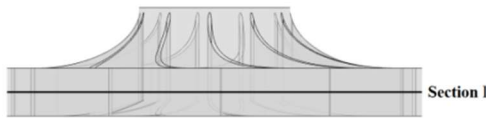


Fig. 5. Location diagram of Section I.

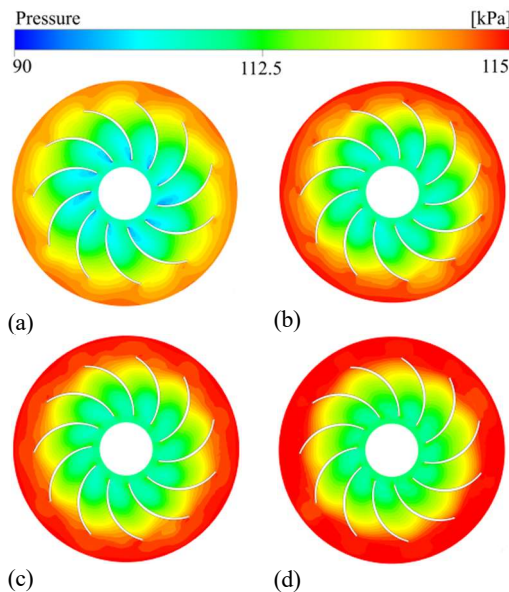


Fig. 6. Pressure distributions at the middle-section of the impeller outlet (section I): (a) Q_n , (b) $0.65Q_n$, (c) $0.47Q_n$, (d) $0.26Q_n$.

Figure 6 describes the pressure distribution on the section I. As described in Fig. 6, it can be seen that the static pressure distribution at this section is relatively uniform at the four working conditions (Q_n , $0.65Q_n$, $0.47Q_n$, $0.26Q_n$). At the rated working condition (Q_n), the low pressure occurs at the inlet of the blade passage, and the static pressure from the inlet to the outlet gradually increases and the pressure gradient gradually decreases, which indicates that the

airflow of the centrifugal blower presents adverse pressure flow in the flow direction and the resistance gradually decreases. At $0.65Q_n$, the area of the low-pressure decreases and the pressure gradient of the front and near edges of the blade increases. At $0.47Q_n$, it can be seen that there is no obvious low-pressure area at the blade inlet, and the high-pressure gradient area is mainly concentrated at the impeller outlet, indicating that there is a large amount of backflow at the outlet. However, when the flow rate reduces to $0.26Q_n$, the pressure significantly rises at the inlet of the impeller. The outlet is completely covered by high pressure, which means that almost no fluid flows out of the outlet. The conveying capacity of the impeller is completely destroyed, leading to the occurrence of rotary stall and surge.

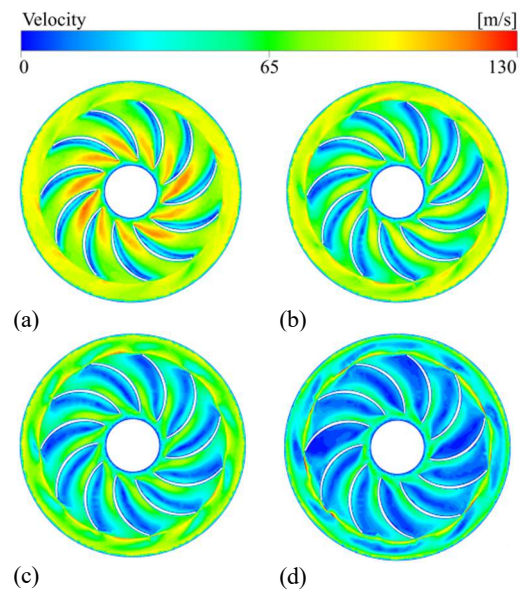


Fig. 7. Velocity distributions at the middle-section of the impeller outlet (section I): (a) Q_n , (b) $0.65Q_n$, (c) $0.47Q_n$, (d) $0.26Q_n$.

Figure 7 shows the relative velocity distribution on the section I at different working conditions. It can be seen that at the rated condition, the velocity in the impeller blade passage varies evenly from the inlet to the outlet, and the relative velocity near the pressure surface (PS) is higher than that on the suction surface (SS). The high velocity gradient is mainly concentrated near the leading edge (LE) of the blade. As the flow rate decreases, the low-speed area on the suction side of the blade gradually expanded and occupied the blade passage at $0.65Q_n$ and $0.47Q_n$ conditions. The low-speed area is one of the signs of reflux and vortex generation. The low-speed area can lead to local flow blockage in the blade passage, preventing fluid from passing through the flow passage smoothly and even generating a large amount of backflow. When the flow rate reduces to $0.26Q_n$, it is obvious that the fluid velocity value decreases relative to the condition of high-quality flow in the whole basin. Each blade passage is filled with a large amount of low-speed flow, causing blockages.

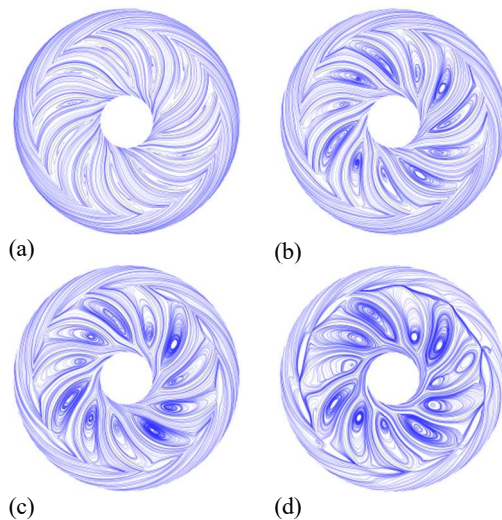


Fig. 8. Streamline distributions at the middle-section of the impeller outlet (section I): (a) Q_n , (b) $0.65Q_n$, (c) $0.47Q_n$, (d) $0.26Q_n$.

A streamline chart is a diagram that represents the flow characteristics of a fluid at a specific period of time, which is an important tool for analyzing the flow trends and flow state of a fluid. Fig. 8 shows the streamline comparison of the section at different working conditions. Illustrated in Fig. 8, we can intuitively see the gradually expanding separation vortex and the gradually blocked impeller passage as the decrease of the flow. In Fig. 8a, it is highly directional in the flow field and the streamline is relatively smooth that the rated condition. Since the relative velocity direction angle of the gas is inconsistent with the designed inlet angle on the blade when entering the passage, a slight prolapsed occurs on the SS of the blade. The flow in the passage is increasingly smooth, and increasingly dense streamlines occur on the PS. In Fig. 8b, the meridional velocity of the gas inlet decreases as the flow rate decreases, and the forward angle of attack formed by the velocity and the blade inlet increases as well. The gas is shot to the working surface, and the non-working surface flow conditions of the blade begin to deteriorate, followed by separating the boundary layer. When the flow rate continues to decrease to the working conditions described in Fig. 8c, the positive angle of impulse continues to increase, and the separation to the flow passage and the outlet direction on the non-working surface gradually expand. As shown in Fig. 8d, the flow continues to decrease, and the separation area expands severely when the positive impulse angle exceeds to a certain critical value. It is obvious that each passage has a large-scale "shape 0" stall vortex near the SS, which almost blocks by the passage. The return of the flow in the low-speed area can also be seen in Fig. 7d, resulting in a greatly weakening of the overflow capacity of the passage. Throughout the rotation stall, generation, separation and shedding of the periodicity will occur for the separation vortex with the time passes by, which will have many adverse effects on the performance of the centrifugal blower.

Figure 9 displays the flow diagram of the centrifugal

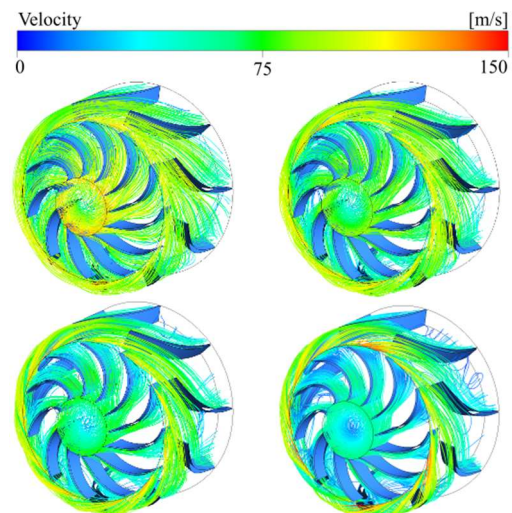


Fig. 9. Three-dimensional streamline of centrifugal blower: (a) Q_n , (b) $0.65Q_n$, (c) $0.47Q_n$, (d) $0.26Q_n$.

blower. At the rated condition, the blower inlet and outlet velocity are greater than other flow, air smoothly enters into the impeller. At the working condition of $0.65Q_n$, there is no streamline at the SS of the impeller blade, which indicates the generation of eddy current. The separation vortex is also generated at the trailing edge (TE) of the SS of the diverter blade. As the air velocity decreases and the pressure increases, a reverse pressure gradient is generated in the blade passage, and the flow resistance of the fluid increases. With the decrease of flow rate, the angle of attack of air flow increases, the reverse pressure gradient increases, and the separation point of air flow moves forward. At $0.47Q_n$, it can be seen that the vortex area of the guide vane expands from the tail to the back of the blade. The vortex at the SS of the impeller blade gradually expands and the flow passage gradually narrows. The impeller inlet speed not only decreases, but also the streamline becomes chaotic at the inlet. At the condition of $0.26Q_n$, the streamline at the inlet is in the shape of vortex, and the interior of the impeller is full of low-speed flow. The separation between the impeller and the diverter is more serious, and some flow passages are blocked. The gas cannot pass through the blade passages smoothly, and even backflow occurs, which seriously reduces the efficiency of the blower.

To announce the motion situation of air flow in flow passage, select the circular intercept line of $0.5R$, $0.75R$ and R (R is the radius of the impeller), shown as Fig. 10. We research the radial air flow motion direction indifferent position of each flow passage within the impeller circle through obtaining the radial velocity vector of air flow on these intercept lines.

Figure 11 is the radial velocity distribution of the different circular intercept lines at different working status. The arrow direction of speed vector represents the motion direction of air flow. From the radial velocity distribution, we can see that a large speed at the entrance position of impeller, which gradually reduce along the outlet direction, and smaller speed at

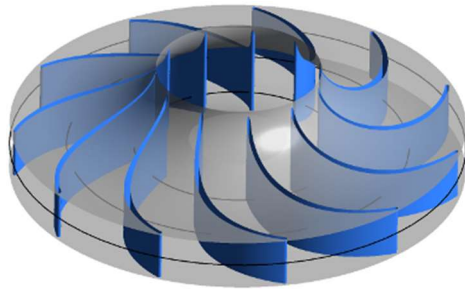


Fig. 10. Position of circular intercept lines in the impeller.

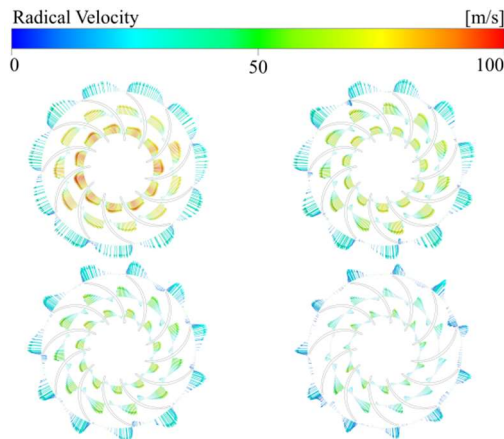


Fig. 11. Radial velocity distribution of the different circular intercept lines in the impeller: (a) Q_n , (b) $0.65Q_n$, (c) $0.47Q_n$, (d) $0.26Q_n$.

vane boundary position. At Q_n working condition, it occurs weak reflow on the $0.5R$ where close to SS of the blade, and return flow increasing at $0.75R$ position, meaning that the weak boundary layer separation at SS. The airflow direction happen deflection due to the influence of the vortex, the main reason is that existing a certain deviation between the inlet angle of the airflow and the blade inlet. At the $0.65Q_n$ working status, the attack angle of airflow decreases with the flow rate decreasing. The obvious reflow appears at the inlet, and the radial velocity also decreases. At the outlet of the impeller, backflows of different sizes occurred at TE of SS. At the $0.47Q_n$, the whole radial velocity vector distribution is close to PS, and the reflow range at the SS increases. Serious backflow occurred at the outlet of the impeller when the flow rate reduces to $0.26Q_n$, and the flow passage is blocked. The sparse distribution of radial velocity vectors on the intercept lines indicates the production of large-scale vortices within the blade passage, and the radial movement of the airflow is less, which may accumulate in the flow passage or the airflow in the circumferential direction due to the backflow. Obviously, low flow is not conducive to the stable operation of the blower.

The one important parameter which represent the turbulent pulse degree in flow field is turbulent kinetic energy. The energy change situation of turbulent vortex in flow field can be directly reflected through turbulent kinetic energy. Figure 12 represents

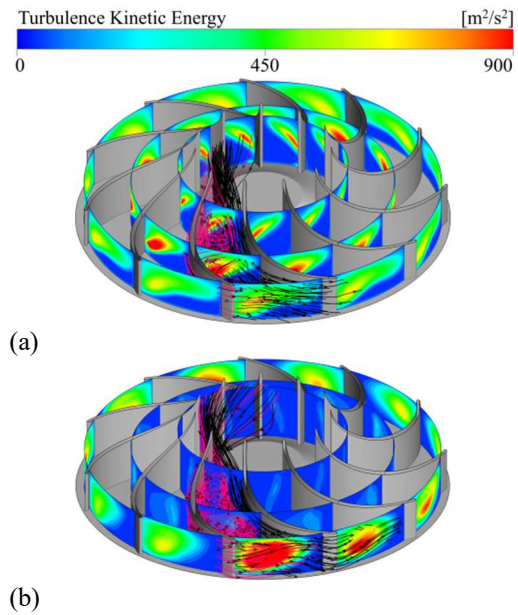


Fig. 12. Turbulent kinetic energy distribute situation on the different circle sections in the impeller: (a) Q_n , (b) $0.26Q_n$.

the turbulent kinetic energy distribute situation on impeller internal different circle section and three-dimensional diagram of one flow passage. When air flows through impeller, the main position which generates turbulent energy loss is near the SS and the front hood at Q_n working status. The turbulent kinetic energy loss at the impeller outlet is slightly reduced. It can be found from the streamline that there is a certain flow separate vortex at impeller inlet, which is located in the middle and upstream of the flow passage, but does not affect the mainstream movement. At $0.23Q_n$, the high turbulent kinetic energy area distributes at impeller outlet position. Viewed from the streamline, there is a large vortex inside the impeller, which occupies most of the flow passage and causes backflow at the outlet. Therefore, the streamline turns rapidly at the outlet of the impeller, which leads to flow pulsation, thus causing flow loss and reducing the efficiency of impeller.

3.3 Time Evolution of Internal Flow Characteristics

In this subsection, the internal flow condition of the centrifugal blower with low flow rate was analyzed based on the numerical calculation method mentioned above through the unsteady numerical simulation.

Figure 13 illustrates an instantaneous pressure and flow diagram on the inner section I of the impeller rotating one lap at 6 different moments, to analyze the change of the inner stall groups of the impeller with time evolution at $0.26Q_n$. T_1 is the time when the impeller rotates for one revolution. It is clearly observed in Fig. 13 that there are stall groups with different shapes and sizes in each flow passage, and three of flow passages are always completely blocked by the stall groups. The stall groups rotate and develop along with the impeller. According to the figure, the pressure in the passage is unevenly

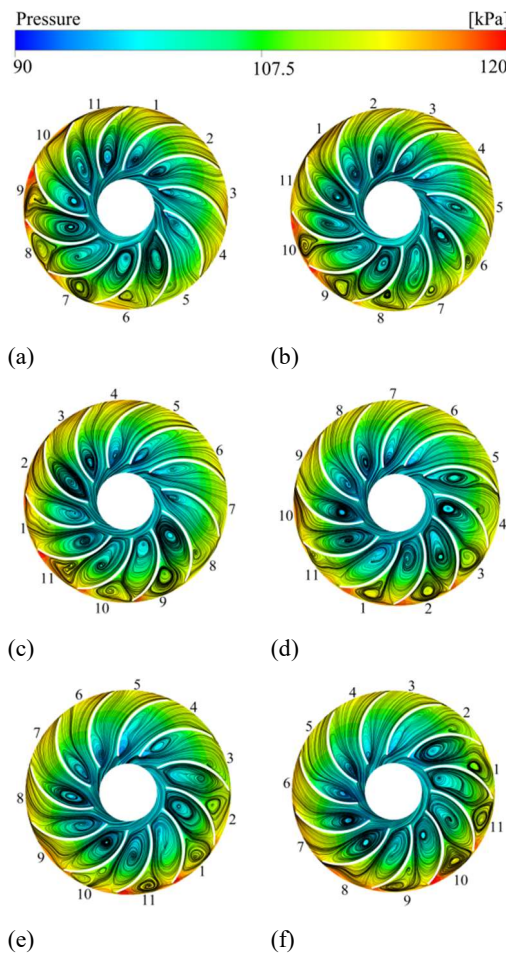


Fig. 13. Time evolution of flow characteristics with on section I at $0.26Q_n$ condition:
 (a) $t=t_0+1T_1/6$, (b) $t=t_0+2T_1/6$, (c) $t=t_0+3T_1/6$,
 (d) $t=t_0+4T_1/6$, (e) $t=t_0+5T_1/6$, (f) $t=t_0+T_1$.

distributed along the peripheral direction, with the high- pressure gradient mainly concentrated in the blocked flow passage. The stall groups can evolve over time and observe the flow passage 1 in Fig. 13a in the early stage. When $T_1/6$ is turned (Fig. 13b), the stall group gradually expands towards the flow passage and the tail edge, indicating that the stall group is isotropic relative to the impeller. At time $t=t_0+3T_1/6$, as the decreased exit velocity and flow rate reduced, a smaller separation vortex occurs near the tail edge of the PS of the flow passage 1, which is clockwise oppositely as the original vortex does. At time $t=t_0+4T_1/6$, we can see that the small separation vortex gradually grows into a big vortex near outlet of the flow passage 1. Then it absorbs the mainstream flow and destroys the mainstream directionality. Eventually it blocks the flow passage at $t=t_0+4T_1/6$, resulting in the air flow that cannot successfully pass through the passage, which indirectly leads to the increased flow angle of the passage 2, repeats the process of the flow passage 1, and propagates to the passage 3 and 4 one by one. Relative to the impeller, the blocked area causes the stall propagate in the opposite direction to the impeller, a phenomenon called rotational stall. The stall group takes the observation target for the flow passage 11 in Fig. 13d.

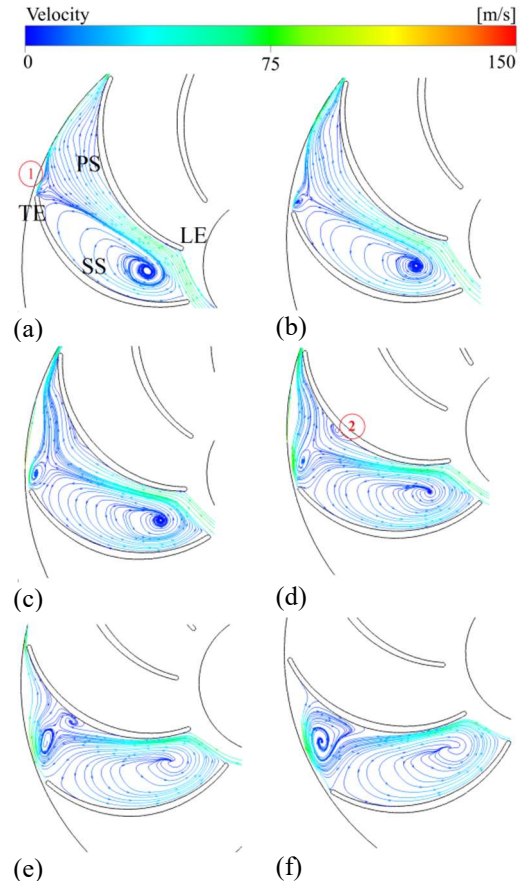


Fig. 14. Time evolution of streamlines of passage 1 at $0.26Q_n$: (a) $t=t_0+19T_1/36$, (b) $t=t_0+20T_1/36$, (c) $t=t_0+21T_1/36$, (d) $t=t_0+22T_1/36$, (e) $t=t_0+23T_1/36$, (f) $t=t_0+24T_1/36$.

As the flow passage 1 blocked, the passage 1 decreases and the pressure decreases. The two vortex groups gradually disperse and decrease at $t=t_0+5T_1/6$. By $t=t_0+T_1$, the passage 11 is no longer blocked and the main stall group becomes smaller and enters the next revolution.

In order to further accurately show the movement and development of the stall groups in the blade passage, more carefully observation has made on the flow passage 1 during the time periods of $t=t_0+3T_1/6$ and $t=t_0+4T_1/6$. Fig. 14 illustrates a transient velocity streamline every 10° , and the stall group shows a significant space-time evolution during this period. In Fig. 14a, it can be seen that there is a large stall vortex in passage 1, occupying two-thirds of the passage. Moreover, its vortex center is near the LE of the blade. A smaller separation vortex 1 (mark ① as shown in Fig. 14a) and a small portion of reflux can be found at TE of SS. In addition, low-speed flows fill most areas, and only a third of the flow passage at the inlet is unblocked. When the impeller rotates 10° to reach the time $t=t_0+20T_1/36$, the separation vortex 1 is gradually formed and the direction is opposite to the rotation direction of the impeller. The backflow at the outlet of the blade passage gradually increases. At time $t=t_0+21T_1/36$, the reflux occupies four-fifths of the outlet. Due to the small flow rate, the angle of attack of the air flow increases with the rotation of

the impeller, resulting in a slight separation phenomenon at PS. The separation phenomenon becomes obvious with time, and another separation vortex 2 (mark ② as shown in Fig. 14d) is formed at $t=t_0+22T_1/36$. At the same time, the separation vortex 1 is gradually expanding. As the flow of the field develops (Fig. 14e), the separation vortex 1 and 2 gradually develop and fuse. At time $t=t_0+24T_1/36$, two separation vortices merge eventually and occupy the entire flow passage with the stall vortex, resulting in serious blockage. Throughout Fig. 14a to f, it can be seen that stall vortex is gradually enlarging, occupying the entire blade passage. And the vortex is slowly shifted from SS to PS.

According to the above results, we can draw a conclusion that the separation vortex always produces on the SS and progressively occupies the flow passage. The separation vortex often drives the downstream fluid while rotating, forming a vortex with the opposite direction of rotation, which is called “outlet vortex”. The outlet vortex is highly close to the PS and eventually completely blocks the flow passage, resulting in the reduction of blower efficiency and surge.

Centrifugal impeller is regarded as the important revolve components in the vacuum cleaner. A large number of vortices at low flow are easily generated due to high-speed revolving motion and caused block. Q-criteria is used to draw the vortex structure to analyze the impeller flow field vortex structure. The equation is as follows:

$$\Omega_{ij} = \frac{1}{2} \left(\frac{\partial u_i}{\partial x_j} - \frac{\partial u_j}{\partial x_i} \right) \quad (9)$$

$$S_{ij} = \frac{1}{2} \left(\frac{\partial u_i}{\partial x_j} + \frac{\partial u_j}{\partial x_i} \right) \quad (10)$$

$$Q = \frac{1}{2} \left(\|\Omega\|^2 - \|S\|^2 \right) \quad (11)$$

where, S_{ij} represents the strain rate tensor, and Ω_{ij} represents the vorticity.

Vortex structures identified by the Q-criteria inside the impeller with 6 instants in a period at the 0.23 Q_n condition are presented in Fig.15. The value of Q is $5 \times 10^8 \text{ s}^{-2}$. It is shown in the picture that the vortex structure of the impeller mainly exists in the downstream part of the impeller passage, which occupies most of the outlet and affects fluid movement. The vortex structure also happen change during the impeller revolving process.

At $t=t_0+1T_1/6$, from the flow passage as marked in Fig.15(a), it can clearly be seen that the vortex structure is generated at LE of SS and expands to PS of the blade. There is no vortex structure on SS of the blade, indicating that the vortex strength is weak. The vortex structure in the outlet of the blade passage is in the shape of a long strip, connecting SS and PS of the blade. When at $t=t_0+2T_1/6$, the vortex at the inlet is broken. The vortex structure downstream of the blade passage continuously merges the surrounding fluid and gradually merges

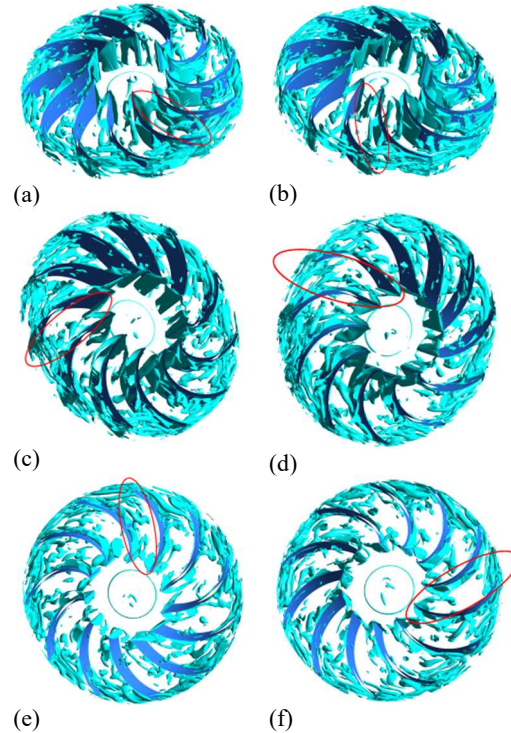


Fig. 15. Time evolution of the vortex structure inside the impeller at 0.26 Q_n condition: (a) $t=t_0+1T_1/6$, (b) $t=t_0+2T_1/6$, (c) $t=t_0+3T_1/6$, (d) $t=t_0+4T_1/6$, (e) $t=t_0+5T_1/6$, (f) $t=t_0+T_1$.

into a complete vortex structure. At $t=t_0+3T_1/6$, the broken vortex at the inlet merges with the vortex in the passage to form an irregular shaped vortex, thus reducing the vortex structure at the outlet. The vortex at the inlet is broken into a sheet shape vortex structure again when at $t=t_0+4T_1/6$. And the vortex group merge and recombine in passage. At the outlet, the separate vortex close to TE of SS continues expanding, forming a sturdy front-end vortex group, which points to PS from SS. The front sturdy vortex group at the outlet develop into a long strip vortex group when at $t=t_0+5T_1/6$, filling the entire outlet. The vortex group at center of passage reduces at $t=t_0+T_1$, and the long stripe shape vortex group at the outlet is broken to form the small stripe shape vortex. The change of the vortex structure inside the impeller is relatively complicated, which starts from TE of SS and expands to PS. Generally, it is broken and reorganized to form a regular vortex structure, and then broken. The period of vortex evolution can be regarded as $2/6T$.

Figure 16 shows the time evolution of streamlines of the span=0.5 in the diverter at 0.26 Q_n . It is distinctly visible in Fig. 16 that four flow passages are always blocked by separation vortices and other passages maintain flowing. Though the diverter is stationary, it is observed that the blocking area is driven from right to left. It can be seen from Fig. 16a that a large number of low-speed flows fill each passage. Meanwhile, the flow passage 2, 3, 4, and 5 are completely blocked. Passage 1 is developing towards a blocked state and a slight separation phenomenon generates near the blade SS close to the blade LE. The small vortex formed is attached

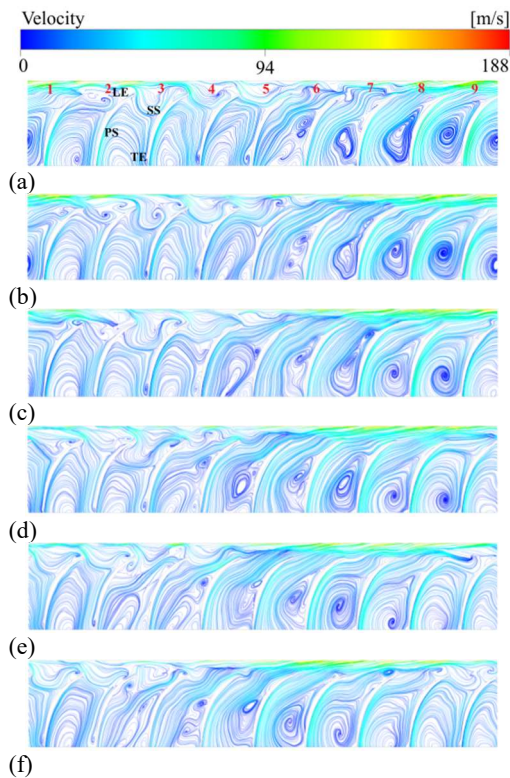


Fig. 16. Time evolution of streamlines of the span=0.5 at 0.26 Q_n . (a) $t=t_0+1T_1/6$, (b) $t=t_0+2T_1/6$, (c) $t=t_0+3T_1/6$, (d) $t=t_0+4T_1/6$, (e) $t=t_0+5T_1/6$, (f) $t=t_0+T_1$

to the blade SS at the inlet of passage 1 at the time $t=t_0+2T_1/6$. At the same time, the fluid in passage 5 gradually becomes smoother, and the separation vortex at SS close to TE gradually expands. As the flow of the field develops, the angle of airflow increases in the flow passage and the main stream is destroyed in Fig. 16d, e, f. A wide flow separation is formed at the inlet to block the flow passage eventually. On the other hand, with the passage of time, the angle of attack of air flow in passage 5 gradually decreases, and the flow can enter the blade passage smoothly. At the time $t=t_0+5T_1/6$, the separation vortex at SS gradually merges with the stall vortex. Finally, there is only one stall vortex in passage 5. In the whole process of rotating stall, the separation vortex will appear, separate and fall off periodically.

3.4 Frequency Domain Characteristics of Pressure Fluctuation

In order to analyze the pressure fluctuation within an impeller, the monitoring points are set up as shown in Fig. 17 according to the previous research characteristics. 6 monitoring points are set near SS along the flow direction in flow passage 1. Each monitoring point is named a_1 to a_6 . The same arrangement has 6 monitoring points near PS, named “b”. Besides, 6 monitoring points are mounted in the middle of the flow passage 2, named c_1 to c_6 . The detailed positions of monitoring points are displayed in Fig. 17. The tenth circle to the twentieth circle is selected to capture the pressure fluctuation characteristics. A fast Fourier transform

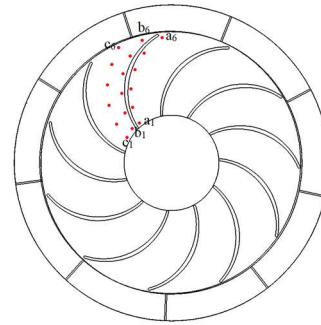


Fig. 17. Position distribution of monitoring points.

(FFT) is applied to the pressure fluctuation of different monitoring points to analyze the frequency characteristics. It can be obtained that the rotation frequency is 1166.67 Hz by rotational speed with 70000 rpm.

The magnitude spectrum of each monitoring point near SS along the flow direction in flow passage 1 at various working conditions are presented in Fig. 18. It can be seen that each monitoring point along SS of blade has the same frequency composition at the same working condition. At the Q_n working condition, the pressure pulsation main frequency of each monitoring point is consistent, which is dominated by the blade passage frequency. Subtle fluctuations can be captured near the low frequency because of a weak flow separation within the impeller, but the flow is generally stable. It can be found that the pressure pulsation amplitude of the monitoring point c_3 in the center of SS is minimal, and gradually increases towards both ends. At $0.65Q_n$, a large number of strong peaks appear in the $8f_n-12f_n$ region and the amplitude increased. This means that the flow interaction inside the impeller is gradually strengthened. As the flow rate continues to decrease, the pressure fluctuation in the low-frequency region is gradually increased at $0.47Q_n$, mainly concentrated in the $3f_n-6f_n$ region, but the pressure amplitude decreases. The flow rate continues to drop to $0.26Q_n$, there are many pressure fluctuation peaks on the pressure fluctuation spectrum and the amplitude fluctuation is more intense. The first characteristic frequency decreases obviously. The amplitude first decreases and then increases along the flow direction. The main reasons are that the flow in the impeller is chaotic, the flow separation is serious, the stall mass blocks the blade passage, and the vortex shedding period around the blade is reduced. The maximum amplitude of the characteristic frequency appears at the monitoring point a_6 , which indicates that the separation flow is more intense at TE of SS.

Figure 19 presents the magnitude spectrum of each monitoring point near PS along the flow direction. At the working condition of Q_n , the amplitude of each monitoring point is mainly concentrated in the blade frequency. The pattern is similar to the pressure pulsation at the suction surface. With the decrease of flow rate, the generation of broadband pulsation in low frequency region will gradually increase, but the main frequency of pressure

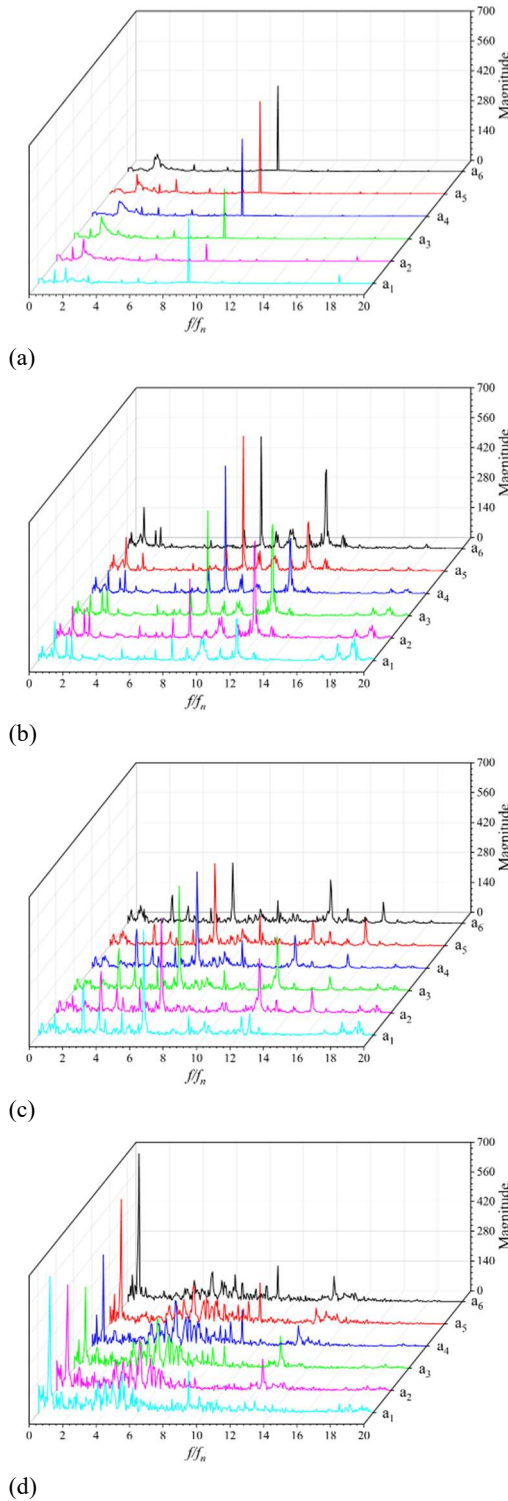


Fig. 18. Magnitude spectrum of each monitoring point along the blade SS. (a) Q_n , (b) $0.65Q_n$, (c) $0.47Q_n$, (d) $0.26Q_n$.

pulsation is the blade passing frequency. At $0.26Q_n$, the amplitude of pressure pulsation shaft frequency accounts for the main part. Along the flow direction, the pressure fluctuation amplitude of the first characteristic frequency shows an obvious decreasing trend. The maximum magnitude of the characteristic frequency appears at the monitoring point b_1 . It indicates that the flow separation is

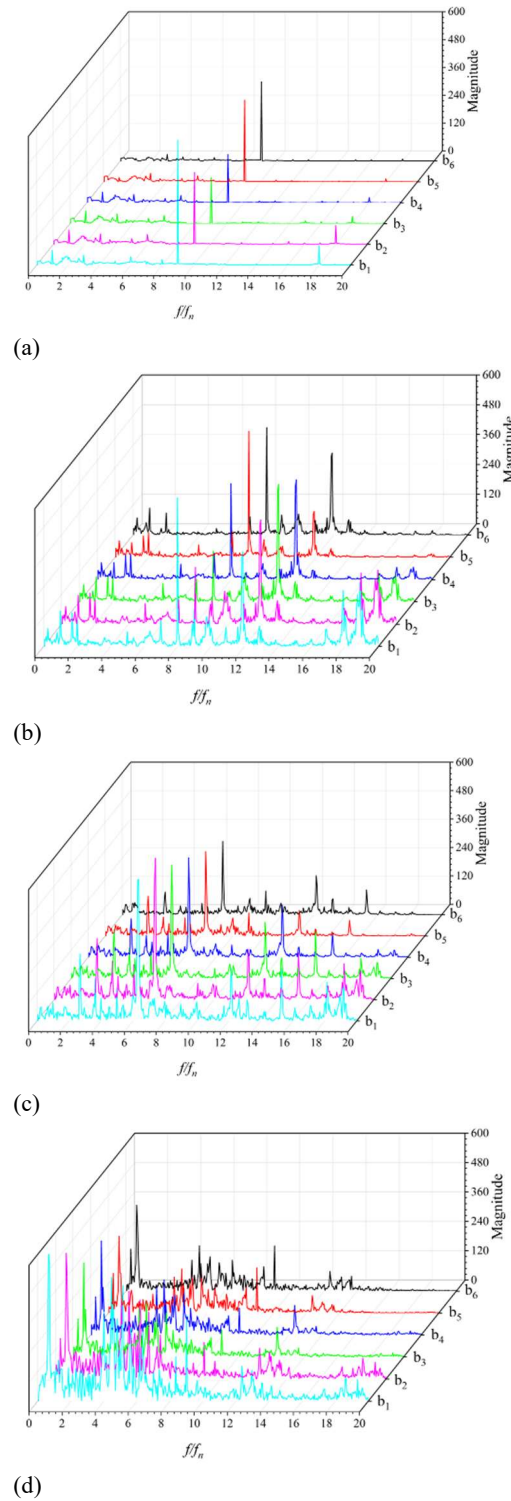
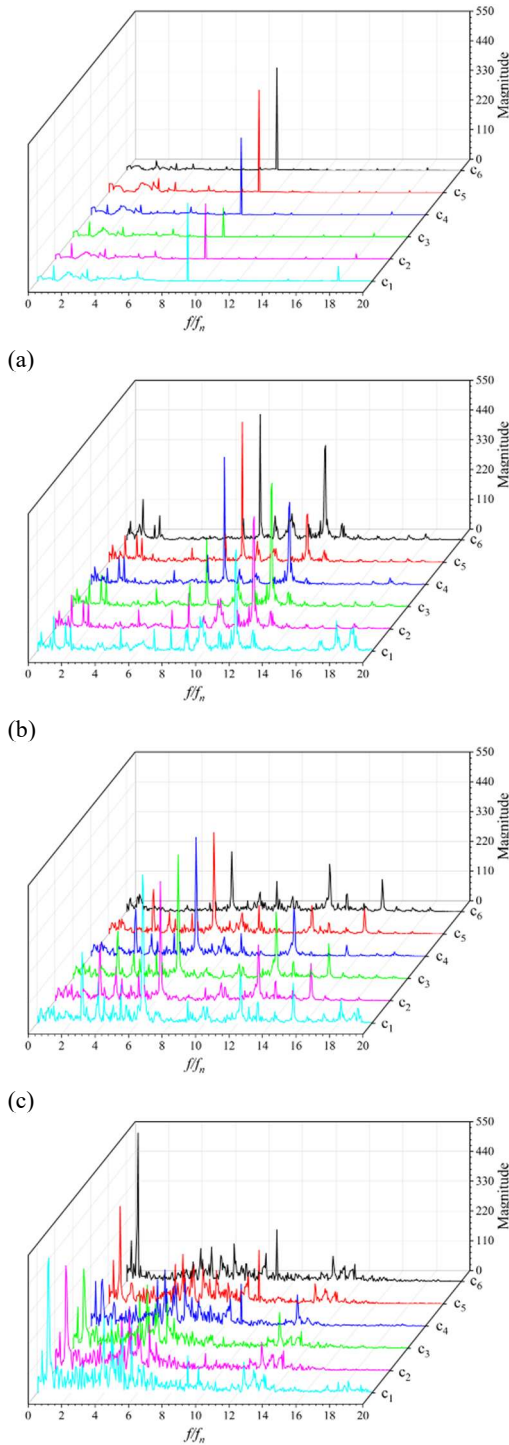


Fig. 19. Magnitude spectrum of each monitoring point along the blade PS. (a) Q_n , (b) $0.65Q_n$, (c) $0.47Q_n$, (d) $0.26Q_n$.

serious near LE of PS. Comparing Fig. 18 with Fig. 19, it can be found that at the same working condition, the pressure fluctuation amplitude of the characteristic frequency at PS is lower than that at SS, which indicates that the unsteady flow phenomenon on SS is more intense.

Figure 20 shows the magnitude spectrum of each



(d)
Fig. 20. Magnitude spectrum of each monitoring point along the flow direction in flow passage 2.
 (a) Q_n , (b) $0.65Q_n$, (c) $0.47Q_n$, (d) $0.26Q_n$.

monitoring point along the flow direction in flow passage 2. At Q_n , the characteristic frequency of each monitoring point is the same, $9f_n$. With the decrease of flow rate, the pulsation in low frequency band increases gradually. At $0.65Q_n$, the amplitude of the first characteristic frequency gradually increases along the flow direction, and the pulsation is the largest at point c_4 , c_5 and c_6 ,

indicating that the flow in the downstream part of the blade passage is chaotic. At the working condition of $0.26Q_n$, the change law and characteristic frequency of each monitoring point in the passage are basically the same as those near SS. But the amplitude of the characteristic frequency decreases obviously.

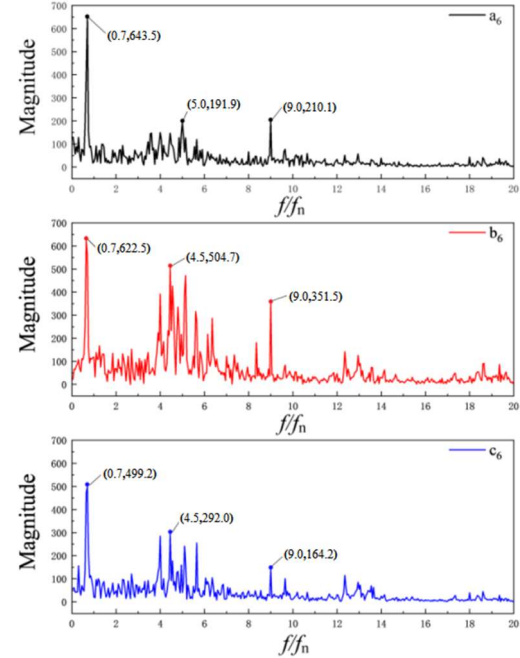


Fig. 21. Magnitude spectrum of monitoring point a_6 , b_6 and c_6 at $0.26Q_n$.

In general, the characterization of pressure fluctuation at the impeller outlet is conducive to a deep understanding of stall and surge at low flow rate. The pressure fluctuations characteristics of impeller outlet near SS(a_6), PS(b_6) and middle(c_6) of the blade are implemented to further study the pressure spectrum analysis at $0.26Q_n$. Fig. 21 presents the magnitude spectrum of three monitoring points at $0.26Q_n$. As described in Fig. 21, the composition of the frequencies is quite complex. The main reason is that a violent rotational stall occurs inside the impeller and the flow is particularly unstable at the condition of low flow rate. The first characteristic frequency is all of $0.7f_n$ while the points are near SS, PS and middle of the blade. However, it is apparent from the figure that the amplitude is maximum on SS of the blade. The second characteristic frequencies of the monitoring points a_6 , b_6 and c_6 respectively are $5.0f_n$, $4.5f_n$ and $4.5f_n$. Besides, the third characteristic frequencies can be observed at $9.0f_n$. Both the second and third characteristic frequencies are the blade passage frequency, caused by the dynamic and static interference between the impeller and the diverter. At the same time, the pressure fluctuations in the blade passage are dominated by low frequency bands. At the low flow conditions, the vortex shedding period around the blade increases, the spectral transport of energy increases, and the turbulent structure of the blade passage noise source caused by air flow is enhanced.

4. CONCLUSIONS

The investigation on centrifugal blower for vacuum cleaner has been performed by CFD calculation software in the study. Some conclusions are obtained.

First of all, the general regularities of static pressure and variable efficiency of this centrifugal blower with flow coefficient are concluded by the analysis and numerical simulation of various working conditions.

Moreover, the steady-state characteristics inside the impeller at different low flow conditions are analyzed from the perspectives of pressure, velocity and streamline. The results show that the flow reduction will cause an increase in the backflow distribution on the working face and the formation of large-scale vortex motion inside the zone. In this paper, the location and reason of vortex formation are discussed in detail, and the phenomenon that the turbulent kinetic energy loss is mainly concentrated at the outlet at low flow conditions is revealed.

In addition, in unsteady simulation at $0.26Q_n$, it can be found that the separation vortex is generated at TE of SS and gradually expands. The separation vortices often drive the downstream fluid while rotating, forming a vortex with the opposite direction of rotation, which blocks the outlet and causes serious loss to the performance of the blower. The evolution shapes of the blade edge vortex and the passage vortex inside the impeller in a period T are displayed. The vortex is always generated at the LE of SS, split, merged into a passage vortex, and shed at the trailing edge of the blade. These vortices can greatly affect the blower flow field and cause corresponding damage.

Furthermore, the analysis of the monitoring points pressure fluctuations and the FFT transformation showed that the unsteady characteristics acting on the impeller gradually increase with the decrease of flow rate. The frequency domain diagram shows that an obvious main peak can be captured in the blade frequency at Q_n , indicating that the fluid is subjected to the periodic action of the impeller. But at low flow, a lot of low frequency clutter is captured, especially at SS. At low flow rate, the vortex shedding period in the impeller increases, and the turbulent structure of the flow passage noise source caused by aerodynamics is also enhanced.

Finally, the steady-flow and unsteady-flow insights can clearly explain the internal flow at low flow conditions of centrifugal blower for vacuum cleaners, and it is helpful to the various engineering design of vacuum cleaner.

ACKNOWLEDGEMENTS

This work was supported by National Natural Science Foundation of China (51906223 and 11872337), the Science and Technology Plan Project of Zhejiang Province (LGG21E060003, LZ22E060002) and the Science and Technology

Key Plan Project of Zhejiang Province (2021C01049, 2020C04011).

REFERENCES

- Bai, L. and Z. Song (2020). Simulation analysis of multistage vacuum cleaner fan flow filed. *Mechanical Design and Manufacturing* 11, 224-227.
- Borello, D., A. Corsini, G. Delibra, M. Fiorito and A. G. Sheard (2013). Large-eddy simulation of a tunnel ventilation fan. *Journal of Fluids Engineering* 135(7), 071102, 1-9.
- Chun, G., M. Wang and Z. Tang (2011). A Study on surge and stall under the interaction of parallel axial flow fan in tunnel. *Noise & Vibration Worldwide* 42(11), 9-14.
- Gan, J., F. Liu, M. Liu and K. Wu (2008). The unsteady fluctuating pressure and velocity in a cross flow fan. *Journal of Thermal Science* 17(04), 349-355.
- Gao, F. and W. Zhong (2012). Numerical simulation and experiment research on pressure fluctuation and aerodynamic noise field of a multi-blade centrifugal fan. *Advanced Materials Research* 1670, 468-471.
- Ishida, M., T. Surana, H. Ueki and D. Sakaguchi (2005). Suppression of unstable flow at small flow rates in a centrifugal blower by controlling tip leakage flow and reverse flow. *Journal of turbomachinery-transactions of the ASME* 7(1), 76-83.
- Ming, L., X. Hu, H. Zhang and A. Sun (2018). Optimized design of high-speed centrifugal fan for vacuum cleaner. *Fan Technology*, 60(S1), 7-13.
- Park, J. W., D. Y. Hwang and H. K. Park (2008). Performance improvement of a vacuum cleaner by analysis of the flow around motor. *ASME Fluids Engineering* 10-14, 1167-1171.
- Sandra, V. S., B. T. Rafael, S. M. Carlos and G. P. José (2005). Unsteady flow pattern characteristics downstream of a forward-curved blades centrifugal fan. *Journal of Fluids Engineering* 123, 265-70.
- Shen, Y., Y. Li, H. Wang, W. Shen, Y. Chen and H. Si (2019). Numerical simulation and performance optimization of the centrifugal fan in a vacuum cleaner. *Modern Physics Letters B* 33(35), 1950440, 1-21.
- Sundstrm, E., B. Semlitsch and M. Mihescu (2018). Generation mechanisms of rotating stall and surge in centrifugal compressors. *Flow, Turbulence and Combustion* 100(3), 705-719.
- Wang, Z., Y. Wei and Y. Qian (2020). A bounce back-immersed boundary-lattice Boltzmann model for curved boundary. *Applied Mathematical Modelling* 81, 428-440.
- Wei, Y., L. Zhu and Z. Wang (2019). Numerical and

- experimental investigations on the flow and noise characteristics in a centrifugal fan with step tongue volutes. *ARCHIVE Proceedings of the Institution of Mechanical Engineers Part C Journal of Mechanical Engineering Science* 234(15), 2979-2993.
- Wolfram, D. and T. Carolus (2010). Experimental and numerical investigation of the unsteady flow field and tone generation in an isolated centrifugal fan impeller. *Journal of Sound & Vibration* 329(21), 4380-4397.
- Yang, H., W. Zhang and Z. Zhu (2019). Unsteady mixed convection in a square enclosure with an inner cylinder rotating in a bi-directional and time-periodic mode. *International Journal of Heat and Mass Transfer* 136, 563-580.
- Yang, J., L. Meng, L. Zhou, Y. Luo and Z. Wang (2013). Unsteady internal flow field simulations in a double suction centrifugal fan. *Engineering Computations* 30(3), 345-356.
- Younsi, M., F. Bakir and S. Kouidri (2007). Numerical and experimental study of unsteady flow in centrifugal fan. *Proceedings of the Institution of Mechanical Engineers Part A Journal of Power and Energy* 221, 1025-36.
- Zhang, W., Y. Lu, W. Gong and G. Xi (2013). The performance impact of half-high diffuser in centrifugal fan for vacuum cleaner. *Electrical Equipment* S1, 633-637.
- Zhang, J., W. Chu, H. Zhang, Y. Wu and X. Dong (2016). Numerical and experimental investigations of the unsteady aerodynamics and aero-acoustics characteristics of a backward curved blade centrifugal fan. *Applied Acoustics* 110, 256-267.
- Zhang, L., R. He, X. Wang, Q. Zhang and S. Wang (2019a). Study on static and dynamic characteristics of an axial fan with abnormal blade under rotating stall conditions. *Energy* 170, 305-325.
- Zhang, W., X. Li and Z. Zhu (2019b). Quantification of wake unsteadiness for low-Re flow across two staggered cylinders. *ARCHIVE Proceedings of the Institution of Mechanical Engineers Part C Journal of Mechanical Engineering Science* 233, 19-20.
- Zhang, Y., Q. Chen, Y. Zhang and X. Jia (2011). Numerical simulation and experiment research on aerodynamic characteristics of a multi-blade centrifugal fan. *Advanced Materials Research* 1380, 317-319.
- Zhou, P., J. Dai, Y. Li, T. Chen and J. Mou (2018). Unsteady flow structures in centrifugal pump under two types of stall conditions. *Journal of Hydrodynamics* 30(6), 1038-1044.